Synthesis and Characterization of Nanometric Iron and Iron-Titanium Oxides by Mechanical Milling:

Electrochemical Properties as Anodic Materials in Lithium Cells

Julián Morales,[a,*] Luis Sánchez,[a,z] Francisco Martín,[b] Frank Berry,[c] and Xiaolin Ren[c]

[a]*Departamento de Química Inorgánica e Ingeniería Química, Facultad de Ciencias, Campus de Rabanales, Universidad de Córdoba, 14071 Córdoba, Spain*
[b]*Laboratorio de Materiales y Superficie (Unidad Asociada al CSIC), Universidad de Málaga, Málaga, Spain*
[c]*Department of Chemistry, The Open University, Milton Keynes MK7 6AA, United Kingdom*

Nanometric mixed iron-titanium oxides were prepared by mechanical milling with a view to determining their ability to act as anodic materials in lithium cells. At a TiO_2/Fe_2O_3 mole ratio of 0.4, a solid-state reaction occurs that leads to the formation of Fe_5TiO_8, which possesses a spinel-like structure; at lower ratios, however, the structure retains the hematite framework. Li/g -Fe_2O_3 cells exhibit poor electrochemical reversibility; by contrast, Ti-containing electrodes possess improved cycling properties. Changes in the electrodes upon cycling were examined by X-ray photoelectron spectroscopy (XPS). XPS data confirm the participation of electrolyte in the electrochemical reaction and the different type of electrochemical reversibility exhibited by samples. Both processes were influenced by the presence of titanium. Titanium dioxide, in the presence of iron oxides, seems to be inactive to the electrochemical process. Based on the step potential electrochemical spectroscopy (SPES) curves and photo-electron spectra obtained, the presence of Ti increases the reversibility of the redox reactions undergone by the electrolyte during discharge/charge processes. The increased active-material/electrolyte/inactive-material interaction which is reported here offers new perspectives for the use of well-known transition oxides as anode materials in Li-ion batteries.
© 2005 The Electrochemical Society. [DOI: 10.1149/1.1972812] All rights reserved.

In the last decade, the search for alternative anodic materials to replace carbon-based materials in Li-ion batteries has primarily focused on systems reversibly alloying with lithium at low potentials such as tin[1-3] and silicon[4] compounds, and intermetallic alloys.[5-7] A new approach to the development of anodic materials was recently reported by Poizot et al.,[8] however. Their thorough revisiting of the electrochemical reduction of 3d-transition metal oxides (M_xO_y, where M = Co, Ni, Cu, Fe) revealed that the complete reduction of these oxides produces composite materials consisting of nanometric clusters of the metal dispersed in an amorphous Li_2O matrix. A simple mechanism was put forward to account for the electrochemical reversibility observed[8-10] that is summarized by the following reaction

$$M_xO_y + 2yLi \rightleftarrows xM + yLi_2O \qquad [1]$$
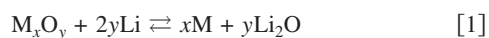
The nanometric/composite nature of the reduced electrodes promotes the decomposition of Li_2O during the oxidation process. Based on the reversibility of this reaction, transition metal oxides can retain capacity values as high as 700 mAh/g on extended cycling, i.e., roughly twice as high as those provided by graphite-based anodic materials (theoretical gravimetric capacity 372 mAh/g). Such attractive properties prompted the exploration of various transition metal oxides including Co_3O_4,[10-13] Fe_2O_3,[14] $LiFeO_2$,[15] Li_5FeO_4,[15] NiO,[8,16] CuO,[9,17] and Cu_2O[9,18] as anodic materials for Li-ion batteries.

Iron oxides are among the most interesting materials for use in commercial Li-ion batteries on economic and environmental grounds. Morzilli et al. were the first to describe the ability of Fe_2O_3 to react with lithium in a lithium cell to form phases of nominal composition $Li_6Fe_2O_3$.[19] However, its low reversible capacity, ca. 0.5 Li, restricted its use as an anodic material. There have been further reports of more efficient use of Fe_2O_3 as a negative electrode material; however, the delivered capacity invariably dropped rapidly with cycling.[20-22]

This paper demonstrates, for the first time, the favorable effect of the addition of TiO_2 to Fe_2O_3 on its electrochemical properties in lithium cells. The mixed transition metal oxides formed are activated by prolonged grinding. This procedure not only provides nanometric particles, but also can induce solid-state reactions that alter the host structure. In addititon, the presence of titanium improves the cycling properties of the electrodes and cell performance.
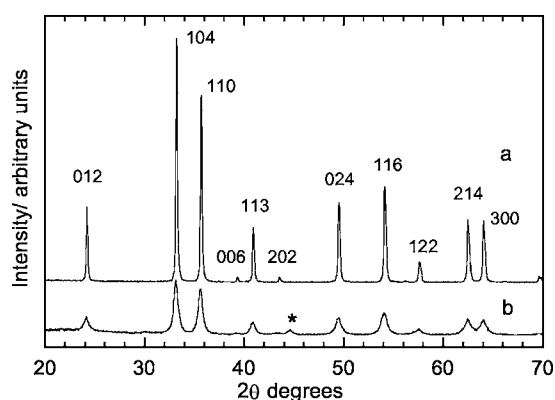
Experimental

Iron-titanium oxides were prepared from stoichiometric mixtures of commercial grade Fe_2O_3 and TiO_2. The mixtures were dry milled in the air in a Restch PM400 planetary ball mill using stainless-steel vials (250 mL) and balls (20 mm) at 200 rpm for 135 h.

X-ray powder diffraction (XRD) patterns were recorded on a Siemens D5000 X-ray diffractometer, using Cu Kα radiation and a graphite monochromator, in steps of 0.02° and 1.2 s. Transmision electron microscopy (TEM) images were obtained with a JEOL 2000fx microscope.

X-ray photoelectron spectra were recorded on a Physical Electronics PHI 5700 spectrometer using non-monochromated Mg Kα radiation ($h\nu$ = 1253.6 eV) and a hemispherical analyzer operating at constant pass energy of 29.35 eV. Spectra were recorded with the X-ray generator operated at 15 kV and 20 mA. The energy scale of the spectrometer was calibrated by using the Cu $2p_{3/2}$, Ag $3d_{5/2}$, and Au $4f_{7/2}$ photoelectron lines at 932.7, 368.3, and 84.0 eV, respectively. The vacuum in the analysis chamber was lower than 10^{-9} mbar. Binding energies were corrected by using that for C 1s of adventitious carbon (and the methyl group) fixed at 284.8 eV. Samples were mounted on a holder without adhesive tape and kept under high vacuum in the preparation chamber overnight prior to transfer to the analysis chamber of the spectrometer. Survey spectra over the range 0-1200 eV were recorded at a 187.85 pass energy, each region being scanned several times to ensure an adequate signal-to-noise ratio. A 3 × 3 mm sample area was sputtered with 4 keV Ar^+; the sputter rate was assumed to be ~0.3 nm min^{-1} as determined for Ta_2O_5 under identical sputtering conditions. Spectra were processed by using PHI-Access V.6 and Multipak software, both from Physical Electronics. High-resolution spectra were fitted after Shirley background correction and satellite subtraction. Surface atomic concentrations were determined from peak areas, using Shirley background subtraction and sensitivity factors provided by the

* Electrochemical Society Active Member.
z E-mail: luis-sanchez@uco.es

Figure 1. XRD patterns for (a) α-Fe$_2$O$_3$ and (b) milled α-Fe$_2$O$_3$ (g-Fe$_2$O$_3$).

Figure 2. XRD patterns for iron-titanium oxides obtained by mechanical milling. (a) Sample A. (b) Sample B. Inset: XRD patterns obtained after calcination at 700°C for samples (c) A and (d) B. [The XRD pattern for standard rutile is shown as straight lines.]

spectrometer manufacturer (Physical Electronics, Eden Prairie, MN). In order to avoid reduction of higher metallic oxidation states by X-rays, spectra were collected with short acquisition times. Ex situ XPS measurements were performed on the acetonitrile-washed pellet from the dismantled cell. All manipulations were done under an argon atmosphere; also, a special glove box connected to the spectrometer antechamber allowed samples to be transferred to the spectrometer without direct contact with air.

Electrochemical measurements were performed in two electrode cells, using lithium as a counter electrode. The electrolyte was Merck battery electrolyte LP 40 (EC:DEC = 1:1 w/w, 1 M LiPF$_6$). Electrode pellets were prepared by pressing, in an stainless-steel grid, ca. 4 mg of active material with polytetrafluoroethylene (PTFE) (5 wt %), and acetylene black (10 wt %) at 4 ton. Galvanostatic tests were conducted under various galvanostatic regimes from C to $C/6$ (C being defined as 1 Li$^+$ exchanged in 1 h). Step potential curves were recorded at 2.5 mV/0.22 h per step. All electrochemical measurements were controlled via a MacPile II potentiostat-galvanostat.

Results and Discussion

Figures 1 and 2 show the X-ray powder diffraction patterns for α-Fe$_2$O$_3$ and the iron-titanium oxides. Milling of α-Fe$_2$O$_3$, hereafter referred to as g-Fe$_2$O$_3$, decreased particle crystallinity as reflected in the smaller, broader peaks obtained (Fig. 1b). Iron-titanium oxides were prepared by mixing TiO$_2$ and α-Fe$_2$O$_3$ in mole ratios of 0.25 and 0.4 (samples A and B, respectively). Most peaks in the XRD pattern for sample A can be ascribed an α-Fe$_2$O$_3$-related structure (Fig. 2a). The small reflection at 27.5° 2θ coincides with the stronger reflection of the rutile form of TiO$_2$. Mechanical milling of the material with the higher proportion of titanium altered the hematite structure. Thus, sample B crystallized in a new phase, the spacings of which are consistent with those of the ulvospinel Fe$_5$TiO$_8$ [ICDD card no. 25-417], Fig. 2b. The small peak near 45° 2θ (marked with an asterisk), that was quite well-defined for some samples, was ascribed to an impurity coming from the mill balls and jar.

The unit cell dimensions of g-Fe$_2$O$_3$, samples A and B, are shown in Table I. Two differences between the α-Fe$_2$O$_3$-related structures are worth special note. Thus, the unit cell of the Ti-containing phase is slightly expanded. An explanation based on the
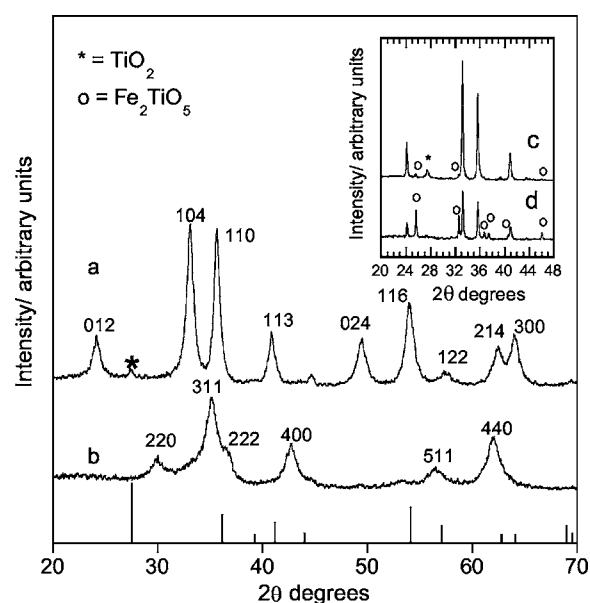
substitution of Fe^{3+} by Ti^{4+} would be inconsistent with the smaller size of Ti^{4+} (the Fe^{3+} and Ti^{4+} ionic radii are 0.78 and 0.74 Å, respectively). A potential substitution of Fe^{3+} by Ti^{3+}, consistent with both structural and ionic radius size considerations, is unlikely as Ti^{4+} can hardly have been reduced to Ti^{3+} under the experimental conditions of the grinding process. The other noteworthy difference is that the intensity of the peaks with an l index of zero [reflections (*110*) and (*300*)] increased with increasing grinding (the calculated I_{110}/I_{104} values were 0.7, 0.85, and 0.98 for standard α-Fe$_2$O$_3$, g-Fe$_2$O$_3$ and sample A, respectively. A similar trend was observed for the I_{300}/I_{104} ratio). This was particularly so in the titanium-containing sample. This phenomenon has previously been observed[23] and suggests a pronounced preferred orientation in the samples typical of an acicular habit, with elongation along ⟨001⟩ that boosts *hk0* reflections. The phase composition of sample A was calculated by subjecting the XRD data to Rietveld refinement[24] using the GSAS software suite.[25] Based on the results, the materials contain ca. 96% α-Fe$_2$O$_3$ and 4% rutile TiO$_2$. Therefore, a significant fraction of TiO$_2$ goes undetected by X-radiation, either because the milling process renders it amorphous or because it is occluded by hematite particles.

Calcination of samples A and B at 700°C for 24 h shed some light on the structural changes caused by grinding. Thus, the ulvospinel phase found in sample B decomposed into hematite and pseudobrookite, Fe$_2$TiO$_5$, under these conditions (see the inset in Fig. 2d), the former being the major component. No reflections corresponding to the rutile phase were observed. By contrast, the XRD pattern for calcined sample A exhibited reflections typical of α-Fe$_2$O$_3$, rutile TiO$_2$, and Fe$_2$TiO$_5$ (Fig 2c). The presence of rutile, which was a minor component in the pristine sample, suggests that this phase does not react with α-Fe$_2$O$_3$ at this temperature level.

Table I. Unit cell parameters and crystallite size (nm) for ground iron and iron-titanium oxides.

Sample	a, b/(Å)	c/(Å)	V (Å^3)	L_{104}	L_{024}	L_{400}	L_{440}
g-Fe$_2$O$_3$	5.036(1)	13.754(1)	261.6	25	21	-	-
A (0.8Fe$_2$O$_3$·0.2TiO$_2$)	5.039(1)	13.810(4)	262.9	15	13	-	-
B (Fe$_5$TiO$_8$)	8.46(1)	8.46(1)	605.4	-	-	11	10
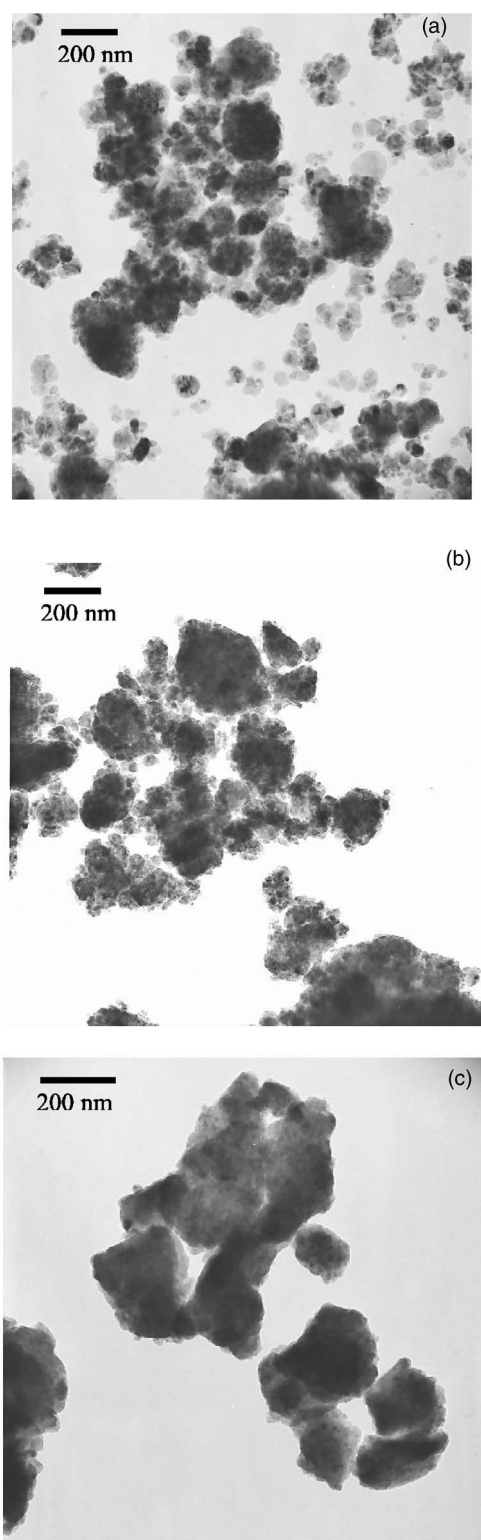
Figure 3. TEM images of (a) g-Fe$_2$O$_3$; (b) sample A, and (c) sample B.

Figure 4. (a) First galvanostatic curves and (b) specific discharge capacity recorded at different discharge rates for Li/g-Fe$_2$O$_3$ cells.

Therefore, the pseudobrookite phase may form as an amorphous compound during grinding or by reaction of amorphous or occluded TiO$_2$ particles with hematite particles during heating.

Figure 3 shows selected transmission electron micrographs for the iron-titanium oxides A and B. The micrographs for A are similar to those for α-Fe$_2$O$_3$ and show agglomerates of nanoparticles ca. 20 nm in 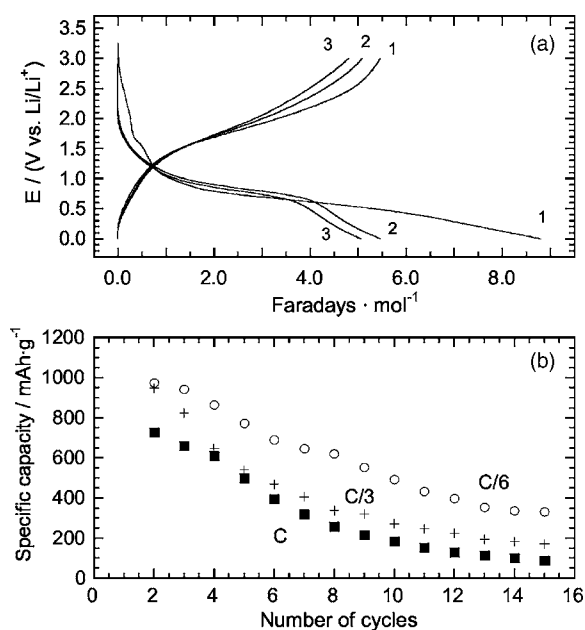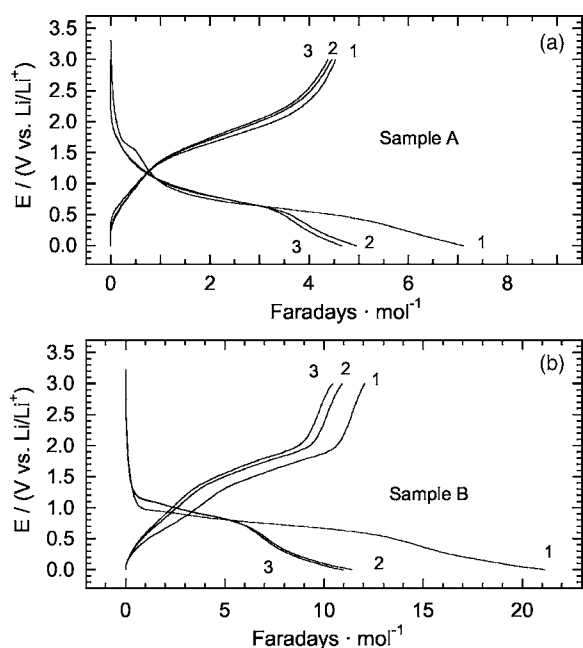size. Sample B, with a different structure, also possesses a different morphology. Its particles are largely semipolyhedral in shape and 100-300 nm in size. Crystallite size was calculated from the broadening of two X-ray peaks using the Scherrer equation. The values thus obtained are listed in Table I. The crystallite sizes for g-Fe$_2$O$_3$ and sample A are similar to those calculated from the TEM images, which suggests that the particles are formed as single coherent diffracting domains. Sample B behaved differently, and its crystallite size was much smaller than its particle size.

Figure 4a shows the initial discharge-charge curves for g-Fe$_2$O$_3$ as recorded at C/6 rate. The first discharge curve exhibits a high lithium uptake up to a 0.0 V cutoff potential (8.8 Li per Fe$_2$O$_3$ mole, equivalent to 1476 mAh/g). The shape profile is similar to one reported elsewhere.[14] The potential steeply drops on approaching 1.7 V and is followed by a small pseudoplateau at 1.6 V and a smooth drop to a wide plateau in the 0.8-0.5 V range and, finally a sustained decrease to 0.0 V. One salient feature of this curve is the presence of the 1.6 V step, which has only been reported for nanometric hematites and ascribed to Li insertion into the Fe$_2$O$_3$ structure.[14] The plateau is thus consistent with the nanometric nature of the milled hematite. Based on complete reduction of Fe^{3+} $\rightarrow$ Fe^0, one would expect a maximun uptake of 6 Li/Fe$_2$O$_3$.[14,26] The excess capacity appears to derive from electrolyte decomposition in the low-potential region, and the subsequent formation of an organic layer on the surface of the particles. The electrolyte seemingly plays a major role in the overall electrochemical process for these M$_x$O$_y$ electrodes, where the formation of a solid electrolyte interface (SEI) upon discharge at low potentials has been suggested.[8,17]

The charge curve exhibits a strong polarization near 1.4 V, which is followed by a plateau centered at ca. 1.8 V. The amount of lithium removed is about 5.5 Li$^+$ per unit formula, which is somewhat smaller than the 6 lithium atoms at a cutoff voltage of 3.0 V predicted from stoichiometric calculations based on Reaction 1. The amounts of inserted and extracted lithium tend to decrease on cycling. A continuous loss of the specific capacity delivered by the cell on cycling is thus observed, whatever the charge/discharge rate (Fig. 4b). Such poor electrochemical behavior can be ascribed to various factors, namely, the excess capacity spent in the SEI film formation, which is greater for iron oxide particles than for other oxides with better cell performance such as CuO[9] and Co$_3$O$_4$,[10] and to the loss of physical integrity of the electrode on successive cycling.

Figure 5. First galvanostatic curves for (a) Li/sample A and (b) Li/sample B cells.

Figure 6. (a) Specific discharge capacity and (b) charge recovery on cycling of Li/g-Fe_2O_3, Li/sample A, and Li/sample B cells.

Figure 5 shows the galvanostatic curves at $C/6$ regime samples A and B. The faradaic yield was calculated by using a molecular weight defined from the compositions shown in Table I. The electrode from sample A exhibits curve profiles similar to those for g-Fe_2O_3 (Fig. 5a). The lithium uptake is lower, consistent with the smaller amount of iron in this sample. This suggests some electrochemical inactivity in the titanium atoms. The discharge/charge curves for sample B are slightly different from those for sample A (Fig. 5b) and exhibit a similar Li/Fe ratio (4.4 and 4.2 for the first discharge of samples A and B, respectively). The most salient difference is the absence of the small plateau at 1.6 V in the former, consistent with a different structure as noted earlier.

The addition of TiO_2 to α-Fe_2O_3, followed by grinding, improves the reversibility of the electrochemical reaction of hematite (Fig. 6a). The capacity retention values, R_{15}, defined as the ratio between the discharge capacity of the 15th and second cycle, varied from 0.34 for g-Fe_2O_3 to 0.62-0.67 for the titanium-containing oxides. The improvement can be observed more easily by plotting the charge recovery, a term that defines the specific capacity stored by the cell in the charge process in relation to that delivered in the previous discharge process, against the number of cycles (Fig. 6b).

Most of the values for the titanium-containing samples exceeded 95% over the first 16 cycles; by contrast, most of the values for g-Fe_2O_3 were smaller than 90%. The specific capacity values delivered by the electrodes after 15 cycles were 350, 550, and 500 mAh/g for samples g-Fe_2O_3, A, and B, respectively. For comparison, it is better to refer these values to the Fe content. The resulting values would be 507, 887, and 862 mAh/g for samples g-Fe_2O_3, A, and B, respectively. Again, the latter two samples possess a similar capacity despite their having a different structure. This means that the iron content is the main factor for correlating the discharge capacities, and that the electrochemical reaction is related mainly with the $Fe^0 \rightleftarrows Fe^{n+}$ conversion. Thus, Ti facilitates the reverse process as discussed below. The volumetric capacities at the 15 cycle, calculated from the density of rutile, hematite, and ulvospinel, were 2890 and 2490 mAh/cm³ for samples A and B, respectively, and hence substantially greater than that calculated for graphite-based materials (840 mAh/cm³). This advantage may offset the inconvenience of the voltage plateau observed at ca. 0.8 V,
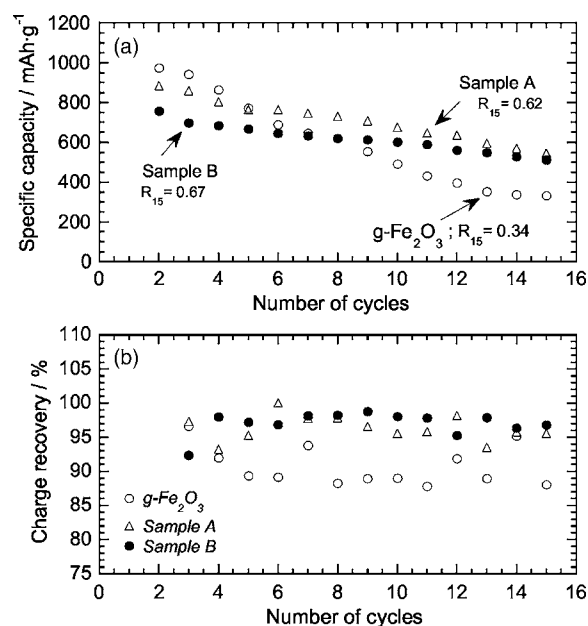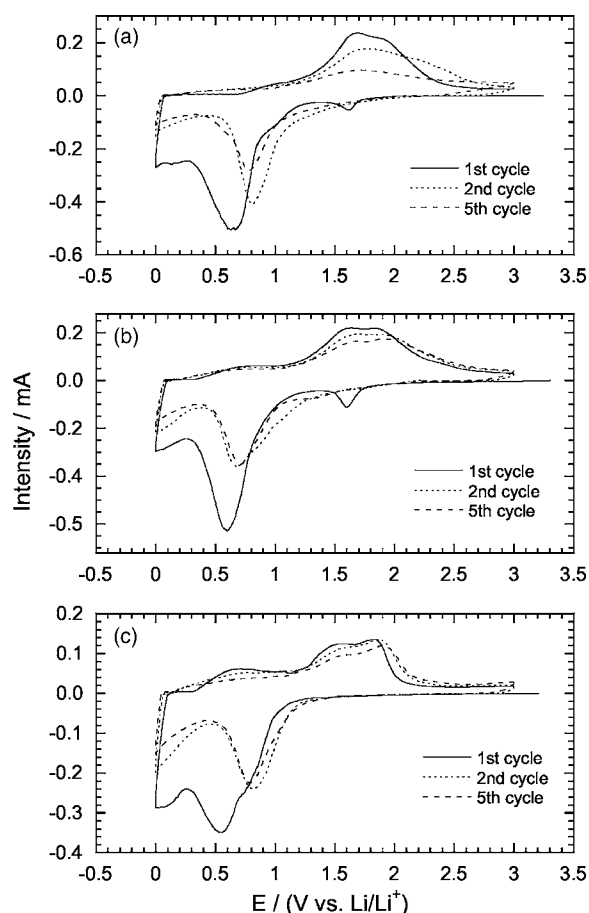
which is somewhat more positive than that for graphite-based materials and make transition metal oxide-based compounds attractive as anodic materials in terms of energy.

In order to shed some light on these electrochemical processes, additional data were obtained by combining the step potential electrochemical spectroscopy (SPES) technique with *ex situ* XRD and XPS measurements. Figure 7 shows the SPES curves for g-Fe_2O_3 and samples A and B. The first cathodic curves for hematite and sample A are very similar, with two well-defined peaks at 1.6 and 0.6 V. The former peak is absent in the corresponding curve for sample B, and the strong peak at 0.6 V is accompanied by a shoulder at the right side of the peak. The first anodic curves for the three samples are similar and include two overlapping broad peaks at ca. 1.5 and 1.9 V. A low, broad signal at ca. 0.7 V was also observed, the intensity of which increased with increasing titanium content. The second and subsequent discharge curves were increasingly similar. The peaks at 1.6 V for g-Fe_2O_3 and sample A, and the shoulder for sample B disappeared. Also, the strong peak shifted to high voltage values. The main changes in the second and subsequent charge curves reflected in a decrease in peak intensity.

The peak at 1.6 V in the cathodic curve can be assigned to lithium insertion into α-Fe_2O_3 and the strong peak at ca. 0.6 V to $Fe^{3+} \rightarrow Fe^0$ reduction. This latter assignation is based on theoretical and experimental electromotive force values for Reaction 1[27] and related systems such as $ZnFe_2O_4$[28] and $Ca_2Fe_2O_5$.[29] Below this peak, one should observe the electrolyte reduction.[17] The presence of titanium seems to facilitate this process; also, its effect on the SPES profile is more pronounced in sample B as a result of its increased titanium content or of a different structure. The disappearance of the peak at 1.6 V in the second discharge indicates that the lithium insertion reaction is irreversible. The double peak observed on charging the cell can be assigned to a change in iron oxidation state in two steps (*viz.*, $Fe^0 \rightarrow Fe^{2+}$ at ca. 1.6 V and $Fe^{2+} \rightarrow Fe^{3+}$ at ca. 1.9 V). These cycling curves reflect the favorable effect of titanium on the reversibility of the electrochemical reaction. The decrease in the peak intensity on cycling for samples A and B (Fig. 7b and c) was much smaller than that for pure hematite (Fig. 7a). Based on reported data,[17] the broad peak at ca. 0.7 V in the anodic scans can be assigned to partial oxidation of the SEI. Interestingly, this peak, which is observed in the titanium-containing oxides, is virtually absent for g-Fe_2O_3. This suggests that the presence of titanium

Figure 7. Step potential curves for the first, second, and fifth electrochemical cycle on (a) $Li/g\text{-}Fe_2O_3$; (b) Li/sample A; and (c) Li/sample B cells.

Table II. Percent atomic composition of the charged electrodes as calculated from the Fe 2p photoemission peak.

Sample	Fe (III)	Fe (II)	Fe (0)
$g\text{-}Fe_2O_3$	30.5	64.3	5.2
A	42.6	54.5	2.9

better comparison with the SPES curves of Fig. 7. The shapes of these two plots are different, consistent with a minor influence of titanium on the electrochemical properties of our samples.

XRD patterns were recorded at the end of the first discharge process and first charge; however, the low signal-to-noise ratio precluded the identification of crystalline phases indicative of the complete degradation of the pristine structure during the electrochemical reduction and the amorphous character of the new oxides formed during the charge process.

Figure 9 shows the Ti 2p and Fe 2p photoemission spectra for the electrodes charged up to 3 V corresponding to $g\text{-}Fe_2O_3$ and sample A following sputtering with Ar^+ for 2 min to improve the signal-to-noise ratio. No signals were detected for the discharged electrodes, even after sputtering with Ar for long periods of time; this suggests that the particles are coated with a thick organic layer originating from the electrolyte decomposition. The Ti 2p profile was fitted to two components (Fig. 9a). The smaller component was assigned to Ti^{3+}, with a low atomic concentration (ca. 5.9%). The major component, which appears at higher binding energy (BE), was assigned to Ti^{4+}. These data confirm the limited participation of Ti^{4+} in the electrochemical process as most titanium atoms remain in the tetravalent state; however, a potential role of the sputtering process as the origin of Ti^{3+} species as recently reported by Hashimoto et al.[31] cannot be excluded. The Fe 2p XPS spectra, Fig. 9b, exhibits multiple components that can be assigned to various oxidation states (Fe^{3+}, Fe^{2+}, and Fe^0). Also, the shake-up satellite structure provides independent, qualitative/quantitative estimation of the relative concentrations of Fe^{3+} and Fe^{2+}.[32] Table II shows the BE and the relative areas of the different components obtained by peak deconvolution using a Gaussian-Lorentzian mixed funtion. Peaks were assigned according to reported values.[32] The main conclusion from these data is the presence of the three oxidation states in both ground hematite and sample A in the charged state, albeit in different proportions. Thus, the titanium-containing sample has a higher content in Fe^{3+} and hence lower contents in Fe^{2+} and Fe^0 (see Table III). Based on these composition data, and on the assumption that iron is completely reduced in the previous reduction process, the overall electrochemical reactions in the first cycle are

$Fe_2O_3+6Li \rightarrow 2Fe+3Li_2O$ Discharge up to 0.0 V
$\rightarrow 0.11Fe+1.29FeO+0.30Fe_2O_3+4.38Li^++0.81Li_2O$
Charge up to 3.0 V

$0.8Fe_2O_3\cdot0.2TiO_2+4.8Li \rightarrow 1.6Fe+2.4Li_2O+0.2TiO_2$
Discharge up to 0.0 V
$\rightarrow 0.05Fe+0.87FeO+0.34Fe_2O_3+0.2TiO_2+3.78Li^++0.51Li_2O$
Charge up to 3.0 V

These stoichiometries are consistent with the corresponding charge profiles for the electrodes (insets in Fig. 9d and e). The amount of lithium calculated from these data in the potential window

may increase the reversibility of the electrochemical reaction undergone by the electrolyte.

The role of titanium in the electrochemical process is controversial. TiO_2 has been proposed as an anode for lithium batteries.[30] The discharge curve exhibited an extended plateau at ca. 1.8 V, which is close to the potential for the small peak in the first cathodic scan of Fig. 7a and b. However, the voltage window used was 2.6-1.2 V and only the first cycle was reported. This prompted us to revisit the Li/TiO_2 system. To this end, we used TiO_2 morphologically similar to the iron-titanium oxides and the same conditions in the electrochemical study. The discharge curve, Fig. 8, exhibits a well-defined potential plateau at 1.75 V followed by a voltage decrease with two subtle slope changes at 1.4 and 0.8 V. The lithium uptake at a 0.0 V cutoff potential is only 1.8 Li per TiO_2, thus indicating incomplete reduction of Ti^{4+} to Ti^{2+}. The initial strong polarization of the charge curve results in a single potential plateau at ca. 2.1 V, whereas the amount of lithium extracted is only 0.5 atoms per TiO_2. This indicates that a significant amount of titanium does not attain the initial Ti^{4+} oxidation state. The plot of the galvanostatic curves in the form of differential capacities (see inset of Fig. 8) allows
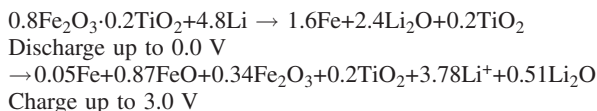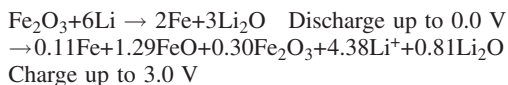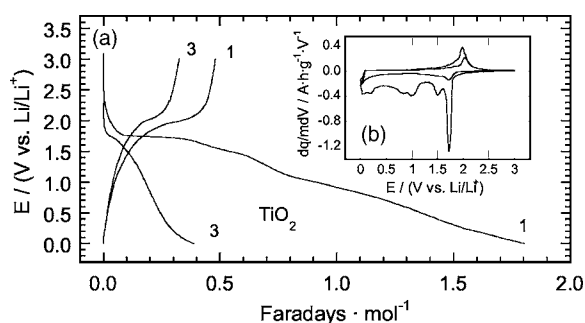
Table III. Binding energies for Fe 2p components. XPS spectra were recorded from the charged electrodes at 3.0 V.

Sample	Fe^{3+}			Fe^{2+}			Fe^0	
	$^2p_{3/2}$	$^2p_{1/2}$	Satellite	$^2p_{3/2}$	$^2p_{1/2}$	Satellite	$^2p_{3/2}$	$^2p_{1/2}$
$g\text{-}Fe_2O_3$	711.1	724.2	718.0	709.7	722.8	714.2	706.7	720.7
A	711.1	724.2	717.3	709.7	722.8	714.2	706.7	720.7

Figure 8. First galvanostatic curves for the Li/TiO$_2$ cell. The inset shows the corresponding differential capacity plot.

1.2–3.0 V, where the Fe^0 → Fe^{n+} oxidation process occurs, is 4.4 and 3.8 Li$^+$ ions for g-Fe$_2$O$_3$ and sample A, respectively. Such good agreement between the XPS and electrochemical data is consistent with the inactivity of TiO$_2$ during the electrochemical process and the preservation of the identity of the iron species during the XPS experiment. In addition, the increased Fe^{3+} content calculated for the titanium-containing charged electrode confirms the favorable effect of this element on cell performance.

The C 1s spectra for the charged electrodes provide additional support for the role played by titanium in the redox reaction of the electrolyte (Fig. 10). The two spectra were fitted to four components with identical binding energies. The peaks were assigned on the basis of literature reports[33] describing the discharge products of CoO up to 0.0 V in lithium cells. The authors assumed the formation of some species proposed by Aurbach et al.[34] ROCO$_2$Li, Li$_2$CO$_3$, and proposed others ones such as RCO$_2$Li and (CH$_2$-CH$_2$O)$_n$. In fact, this latter polymer, the binding energy of which is at 286 eV, disappears on charging. Thus, O bound to C species are formed during the reduction process, probably below 0.5 V. The BE and atomic composition values are listed in Table IV. These results contradict those reported by Dedryvère et al.,[33] as the peak at 286.1 eV assigned to the (CH$_2$-CH$_2$O)$_n$ polymer disappeared during the charge process. The main difference between the two samples is the lower content in O bound to carbon species in the titanium-containing sample (particularly in O-C=O form). Thus, the Ti could either increase the oxidation rate of the reduced species coming from the electrolyte, as reflected in the SPES curves of Fig. 7b and c, or decrease the reduction rate of the electrolyte. Both models would lead to reduction of the SEI layer thickness and result in improved battery performance.

Conclusions

The influence of titanium on the electrochemical behavior of hematite as an anode material in lithium cells was examined. Titanium-containing samples were prepared by following a mechanical milling procedure that provides nanometric particles. At a TiO$_2$/Fe$_2$O$_3$ mole ratio of 0.4, a solid-state reaction occurs that leads to the formation of Fe$_5$TiO$_8$, which possesses a spinel-like structure. The electrochemical reaction with lithium was studied in the poten-

Table IV. Binding energis for C 1s components. XPS spectra were recorded from the charged electrodes at 3.0 V. The values in parentheses correspond to the atomic concentrations.

	C species			
Sample	C-C	C-O	O-C=O	CO$_3^{2-}$
g-Fe$_2$O$_3$	284.8 (55.9)	286.1 (16.9)	287.6 (17.2)	289.8 (9.9)
A	284.8 (60.8)	286.1 (15.8)	287.6 (13.9)	289.8 (9.5)
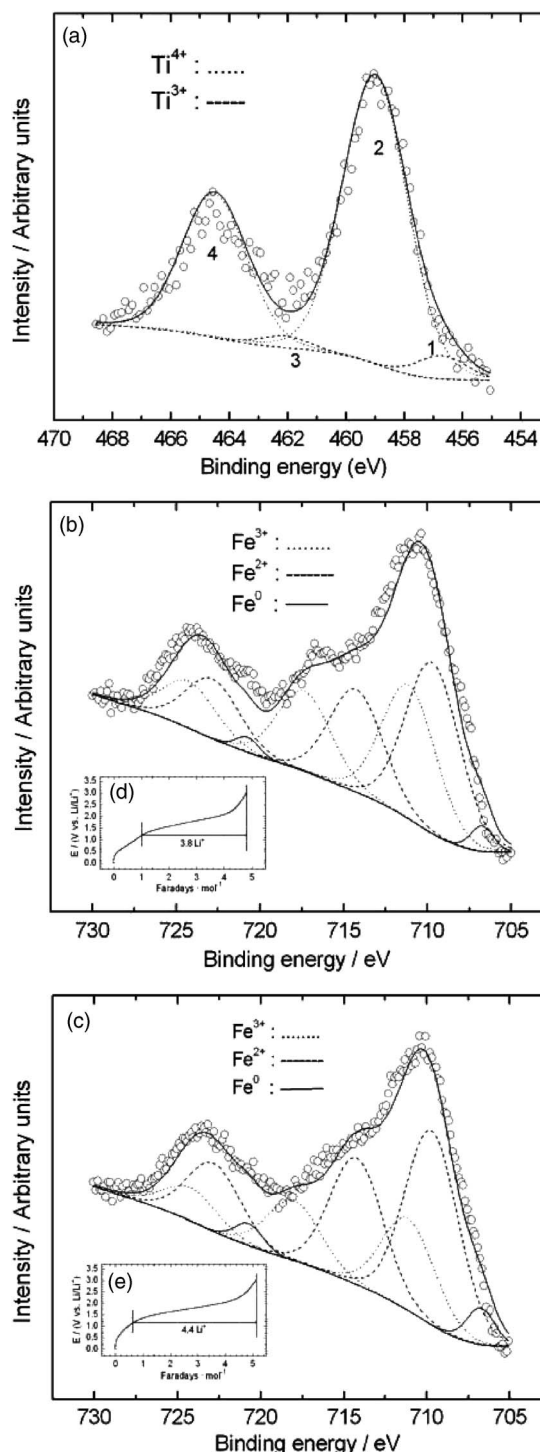
Figure 9. (a) XPS Ti 2p and (b) Fe 2p core level spectra for the electrode from sample A. (c) Fe 2p core level spectra for the g-Fe$_2$O$_3$ electrode. Both spectra were obtained after the first charge up to 3.0 V. Inset: charge curve after complete reduction up to 0.0 V for (d) sample A and (e) g-Fe$_2$O$_3$ electrodes.

tial window 3.0-0.0 V. Under these conditions, the discharge capacities values exceeded those delivered in the total reduction of iron. Therefore, some electrolyte molecules also undergo a reduction process that leads to the formation of an organic layer on the surface of the metal particles. All reduction products are amorphous and fail to regain crystallinity on charging at 3.0 V. The Li/Fe$_2$O$_3$ cell exhibits poor electrochemical reversibility, probably because of the large ca-
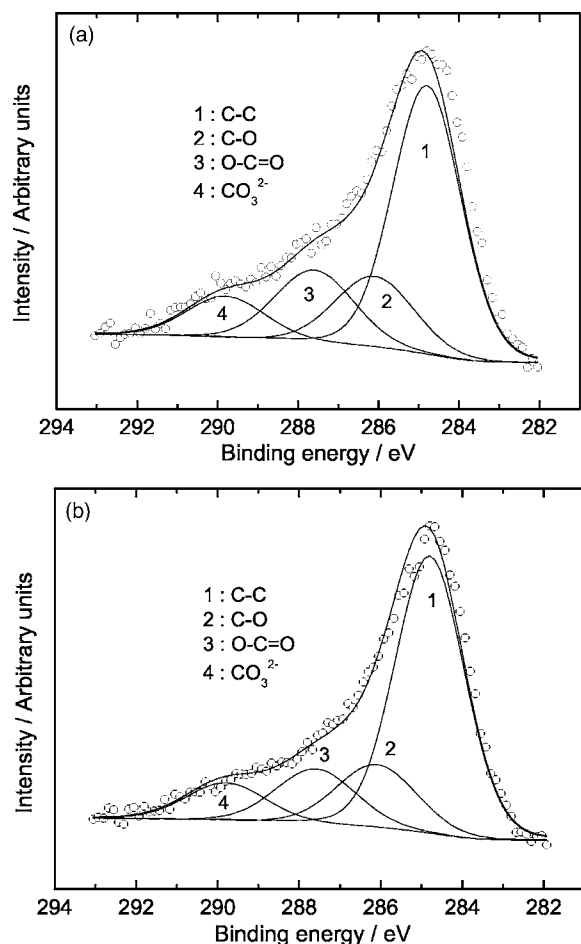
Figure 10. XPS C 1s core level spectra for (a) g-Fe$_2$O$_3$ and (b) sample A electrodes. The spectra were recorded after the first charge up to 3.0 V.

pacity excess used in the electrolyte decomposition. The Ti-containing electrodes exhibit better cycling properties. The XPS data confirm that the discharged electrodes are coated with a thick organic layer which conceals the signal for the metal elements. However, part of this layer is oxidized on charging the cell, thus allowing the analysis of the chemical environmental state of the constituent elements. Both XPS and electrochemical data are consistent with the minor role played by Ti in the charge and discharge values, and also with its favorable effect on the cycling properties of the cell. Thus, the major oxidation state of titanium in the charged electrode is Ti^{4+}, which contradicts the electrochemical calculations. The Fe 2p spectrum for the charged electrodes is consistent with the presence of Fe^{3+}, Fe^{2+}, and Fe^0, the last being the minor species. The atomic concentrations of Fe^{2+} and Fe^{3+} calculated from the photoemission peaks confirm the favorable effect of titanium on the reversibility of the electrochemical reaction. Thus, the Fe^{3+} content is higher in the titanium-containing sample. Also, the presence of titanium increases the reversibility of the redox reactions undergone by the electrolyte during the discharge/charge process as reflected in both the SPES curves and the C 1s spectra for the charged electrodes. Finally, the

use of seemingly inactive TiO$_2$ to the electrochemical process results in a new approach to enhance the electrochemical reactivity of transition metal oxides as anode materials, via an enhancing of the electrolyte redox process.

References

1. Y. Idota, M. Mishima, M. Miyaki, T. Kubota, and T. Misayaka, Eur. Pat. Appl. 651,450 A1 950,503 (1997).
2. I. A. Courtney, W. R. McKinnon, and J. R. Dahn, *J. Electrochem. Soc.*, **146**, 59 (1999).
3. M. Martos, J. Morales, and L. Sánchez, *J. Mater. Chem.*, **12**, 2979 (2002).
4. H. Li, X. Huang, L. Chen, Z. Wu, and Y. Liang, *Electrochem. Solid-State Lett.*, **2**, 547 (1999).
5. J. Yang, M. Wachtler, M. Winter, and J. O. Besenhard, *Electrochem. Solid-State Lett.*, **2**, 161 (1999).
6. O. Mao and J. R. Dahn, *J. Electrochem. Soc.*, **146**, 423 (1999).
7. K. D. Kepler, T. Vaughey, and M. M. Thackeray, *Electrochem. Solid-State Lett.*, **2**, 307 (1999).
8. P. Poizot, S. Laruelle, S. Grugeon, L. Dupont, and J. M. Tarascon, *Nature (London)*, **407**, 496 (2000).
9. S. Grugeon, S. Laruelle, S. R. Herrera-Urbina, L. Dupont, P. Poizot, and J. M. Tarascon, *J. Electrochem. Soc.*, **148**, A285 (2001).
10. D. Larcher, G. Sudant, J. B. Leriche, Y. Chabre, and J. M. Tarascon, *J. Electrochem. Soc.*, **149**, A234 (2002).
11. G. X. Wang, Y. Chen, K. Konstantinov, M. Lindsay, H. K. Liu, and S. X. Dou, *J. Power Sources*, **109**, 142 (2002).
12. Z. Yuan, F. Huang, C. Feng, J. Sun, and Y. Zhou, *Mater. Chem. Phys.*, **79**, 1 (2003).
13. F. Badway, I. Plitz, S. Grugeon, S. Laruelle, M. Dollé, A. S. Gozdz, and J. M. Tarascon, *Electrochem. Solid-State Lett.*, **4**, A115 (2002).
14. D. Larcher, M. Masquelier, C. D. Bonnin, Y. Chabre, V. Masson, J. B. Leriche, and J. M. Tarascon, *J. Electrochem. Soc.*, **150**, A133 (2003).
15. M. N. Obrovac, R. A. Dunlap, R. J. Sanderson, and J. R. Dahn, *J. Electrochem. Soc.*, **148**, A576 (2001).
16. Y. Wang and Q. Z. Qin, *J. Electrochem. Soc.*, **149**, A873 (2002).
17. J. Morales, L. Sánchez, F. Martín, J. R. Ramos-Barrado, and M. Sánchez, *Electrochim. Acta*, **49**, 4589 (2004).
18. J. Morales, L. Sánchez, S. Bijani, L. Gabas, L. Martínez, and J. R. Ramos-Barrado, *Electrochem. Solid-State Lett.*, **8**, A159 (2005).
19. S. Morzilli, B. Scrosati, and F. Sgarlata, *Electrochim. Acta*, **30**, 1271 (1985).
20. B. Di Pietro, M. Matriarca, and B. Scrosati, *J. Power Sources*, **8**, 289 (1982).
21. K. M. Abraham, D. M. Pasquiarello, and E. B. Willstaedt, *J. Electrochem. Soc.*, **137**, 743 (1990).
22. J. Sarradin, M. Ribes, A. Guessous, and K. Elkacemi, *Solid State Ionics*, **112**, 35 (1998).
23. F. J. Berry, C. Greaves, J. McManus, M. Mortimer, and G. Oates, *J. Solid State Chem.*, **130**, 272 (1997).
24. H. M. Rietveld, *J. Appl. Crystallogr.*, **2**, 65 (1969).
25. A. C. Larson and R. B. Von Dreele, Los Alamos National Lab. Report No. LA-UR-86-748 (1994).
26. D. Larcher, C. D. Bonnin, R. Cortes, I. Rivals, L. Personnaz, and J. M. Tarascon, *J. Electrochem. Soc.*, **150**, A1643 (2003).
27. P. Poizot, S. Laruelle, S. Grugeon, and J. M. Tarascon, *J. Electrochem. Soc.*, **149**, A1212 (2002).
28. Y.-N. NuLi, Y.-Q. Chu, and Q.-Z. Qin, *J. Electrochem. Soc.*, **151**, A1077 (2004).
29. N. Sharma, K. M. Shaju, G. V. Subba Rao, and B. V. R. Chowdari, *Electrochim. Acta*, **49**, 1035 (2004).
30. C. Natarajan, K. Setoguchi, and G. Nogami, *Electrochim. Acta*, **43**, 3371 (1998).
31. S. Hashimoto, A. Tanaka, A. Murata, and T. Sakurada, *Surf. Sci.*, **556**, 22 (2004).
32. T.-C. Lin, G. Seshadri, and J. A. Kelber, *Appl. Surf. Sci.*, **119**, 83 (1997).
33. R. Dedryvère, S. Laruelle, S. Grugeon, P. Poizot, D. Gonbeau, and J. M. Tarascon, *Chem. Mater.*, **16**, 1056 (2004).
34. D. Aurbach, B. Markovsky, I. Weissman, E. Levi, and Y. Ein-Eli, *Electrochim. Acta*, **45**, 67 (1999).